Preprints of the 19th World Congress
The International Federation of Automatic Control
Cape Town, South Africa. August 24-29, 2014

Collision Detection and Reaction for a Multi-Elastic-Link Robot Arm ⋆

Jörn Malzahn * **Torsten Bertram** *

* *Institute of Control Theory and Systems Engineering, Technische Universität Dortmund, 44227 Dortmund, Germany; e-mail: joern.malzahn@tu-dortmund.de.*

Abstract: In contrast to the common understanding of robot link elasticity as a detrimental effect the paper presents a novel approach to beneficially exploit the intrinsic link compliance for the detection and reaction to unpredicted collisions between the robot and its environment. The paper employs an inner loop controller to rapidly attenuate structural oscillations. Next, a linear relationship between the actuator joint torques as well as the damped link surface strains is derived to accurately model the residual dynamics. The model is identified for an experimental multi-elastic link robot arm under the influence of gravity. Experimental results are provided using a generalized momentum based technique for the detection and reaction to collisions with fragile objects placed on a force sensor as well as interactions with a human.

1. MOTIVATION

Benosman and Le Vey [2004] point out that the link mass reduction along with link elasticity gains importance in the industrial production due to the ongoing optimization of cycle times and increasing accuracy requirements. Moreover, following Haddadin et al. [2008], mass reduction is a key aspect for the safe physical human-robot-interaction. The cheapest way to reduce the robot mass is probably just to remove link material, which inevitably increases elasticity. Elasticity in the links of multi-body systems such as cherry pickers, automobile concrete pumps, fire rescue turntable ladders and lightweight robots is commonly understood as a detrimental effect, which should be eliminated by mechanical design.

In the context of lightweight robots this paper approaches from the contrary viewpoint on link elasticity. It presents a biologically inspired approach to leverage the intrinsic link compliance for collision detection and reaction. This way, the originally undesired structural property is envisioned to offer promising new perspectives.

Behn et al. [2013] summarize that the vibrissae of rodents "can be moved either passively, or actively through alternate contractions of the intrinsic and extrinsic muscles" connected to the shafts of the individual whiskers. This enables the passive detection of contact forces as well as the tactile scanning of surfaces. Pinnipeds use their whiskers for orientation. They locate and track the hydrodynamic trails of their prey even in murky water (see Miersch et al. [2011]).

While details differ among species, fig. 1 (**a**) illustrates a very basic schematic of a single whisker, the skin realizing the neural connection as well as the actuation mechanism composed of extrinsic and intrinsic muscles. Fig. 1 (**b**) exemplifies a single joint-link-module of an elastic-link robot

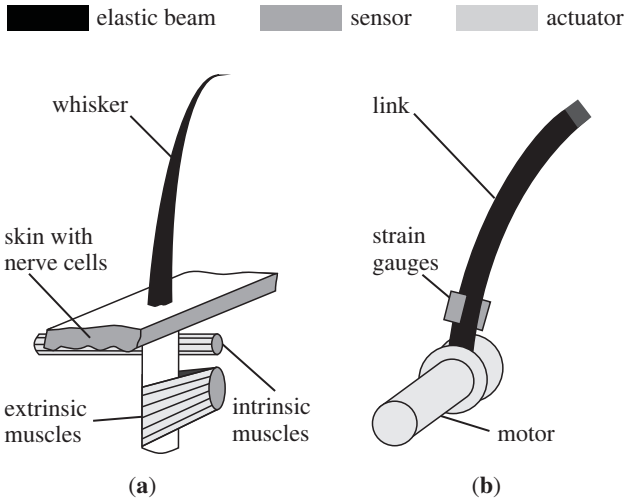

Fig. 1. Schematic comparison of a single whisker (**a**) and a joint-link-module of an elastic-link robot arm (**b**).

with strain gauges and an electrical motor. The module and the whisker share the same structural arrangement. They consist of an elastic beam. The beam is actuated on one end. The sensor for deflection measurement is mounted on the beam surface in the vicinity of this actuator. The similarity suggests that link elasticity can be exploited for collision detection and force control, once the undesired oscillations and static deflections are compensated by advanced control algorithms. To the best of our knowledge, the paper demonstrates the collision detection and reaction for multi-elastic-link arms under gravity for the first time.

The next section summarizes related work, which leads to the oscillation damping control concept used in this contribution. The experimental setup is detailed in section 3. The derivation and identification of the damped arm dynamics are explained in section 4. Section 5 revisits generalized momentum based collision detection. Experi-

⋆ This work is partially funded by the German Research Foundation (DFG, BE 1569/7-1)

mental results for the collision detection and reaction as well as physical human robot interaction are contained in section 6. The paper concludes and gives an outlook in section 7.

2. RELATED WORK

Up to now, the literature concerning elastic-link robots focuses on the oscillation damping and end effector control. Most works are simulative studies. Experiments are frequently limited to single link setups. Setups with oscillations in the horizontal plane exclude static deflections and parameter changes due to gravitational influence. Experimental works on multi-link arms as for example carried out by Mansour et al. [2008] and Malzahn et al. [2011] are comparably rare. Benosman and Le Vey [2004] find the reason for this in "the complexity of the nonlinear multi-link models, since it is difficult even if not impossible to apply directly some *theoretical* closed-loop control strategies, which need closed-form manipulations of these complex system dynamics". The common modeling formalisms elastic beams are collected by Meirovitch [2001]. They involve a truncation of the actually infinite system order to a finite number of assumed modes. For robots varying joint configurations, unpredictable payload changes or physical contacts with the environment alter the boundary conditions to the governing beam partial differential equations. Imperfect clamping adds uncertainty on top of that and renders the derivation and moreover the accurate identification of a holistic multi-elastic-body dynamics model tedious, error prone and computationally intensive.

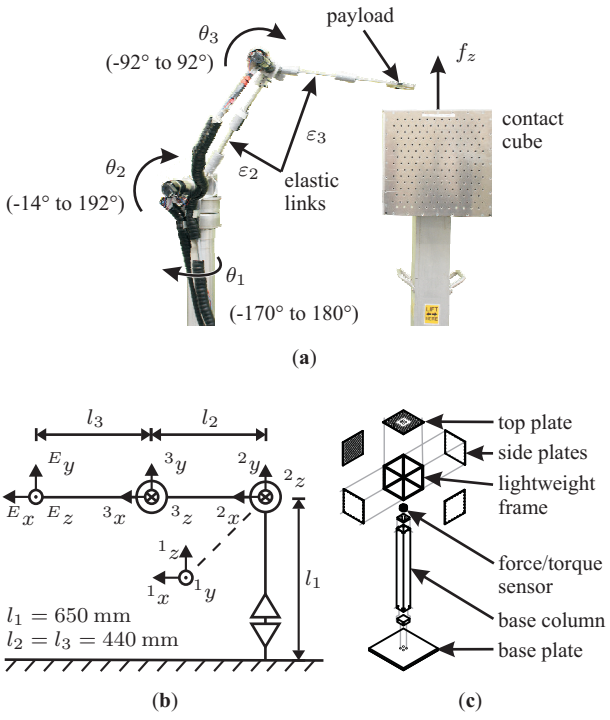

Fig. 2. The three DOF experimental setup TUDOR (**T**echnische **U**niversität **D**ortmund **O**mnielastic **R**obot) and the contact cube for evaluation of collision experiments (**a**). Equivalent rigid body kinematics (**b**) and exploded view of the contact cube (**c**).

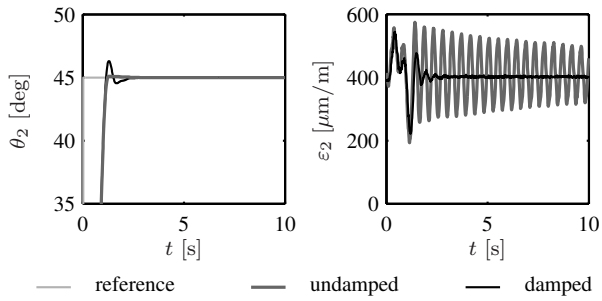

Fig. 3. Oscillation damping during a joint motion from $\boldsymbol{\theta} = [0°, 0°, 0°]^{\mathrm{T}}$ to $\boldsymbol{\theta} = [0°, 45°, -45°]^{\mathrm{T}}$. Second joint angle θ_2 (*left*) and link strain ε_2 (*right*) measured near the second actuator.

Against this background this work follows the decentralized joint angular control strategy proposed by Malzahn et al. [2011]. It waives the need for a holistic coupled multi-input-multi-output dynamics model of the robot. The independent joint angular controllers are augmented by inner oscillation feedback controller, which shapes the closed loop dynamics of each joint-link-module, so that oscillations are rapidly dampened irrespective of their excitation source. Malzahn and Bertram [2014] show that the oscillation feedback paves the way for the drastically simplified modeling of the damped arm dynamics in section 4.

3. EXPERIMENTAL SETUP

The experimental setup TUDOR is depicted in fig. 2 (**a**). The robot is actuated by three brushless DC motors with planetary gears showing less than one degree of backlash. The gear ratios are 156:1, 230:1 and 246:1 for the first, second and third joint. The angular encoders provide 500 impulses per revolution. The cylindrical base houses the first actuator. It turns about the vertical axis ${}^1\mathbf{z}$ by the joint angle θ_1. The other two motors drive the horizontal axes ${}^2\mathbf{z}$ and ${}^3\mathbf{z}$ with the joint angles θ_2 and θ_3. The equivalent rigid body kinematics for TUDOR are sketched in fig. 2 (**b**). The first link body is the mechanical connection between the first two joints. The elastic spring steel blades represent the second and third link. The rectangular cross section of both blades measures 4 mm by 15 mm. The blade mass amounts to 185 g.

According to the respective payload or joint configuration and acceleration, oscillation amplitudes of about 10 cm with eigenfrequencies in the range of 1 to 13 Hz appear in the ${}^2\mathbf{x} - {}^2\mathbf{z}$-plane in parallel to the gravitational acceleration. The strain gauge pairs close to the second and third joints sense both the static deflections due to the arm and payload weights as well as the dynamic oscillations. In the previous works by Malzahn et al. [2011] the static strain readings are cancelled by subtracting the estimated moving average. The mean liberated signal is then fed back to the independent joint oscillation damping controller mentioned in the previous section. A damping result for motion induced oscillations is exemplified in fig. 3.

The contact cube shown in the right of fig. 2 (**a**) incorporates a force-torque sensor as illustrated in the exploded view in fig. 2 (**c**). It serves as a reference for the evaluation of the collision detection and reaction. The edge-length of

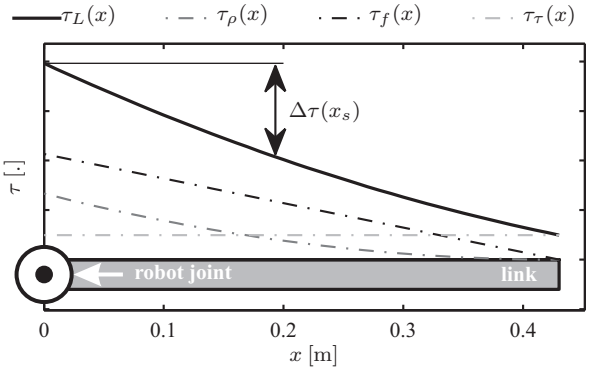

Fig. 4. Qualitative illustration of the load torque distribution $\tau_L(x)$ along a link (*gray bar*) as the superposition of the three components τ_ρ, τ_f and τ_τ.

the cube amounts to 30 cm. The measurement range for the vertical contact force f_z is $\pm 200\,\mathrm{N}$ with a resolution of 0.05 N.

4. DAMPED ARM DYNAMICS

Provided that the inner oscillation damping control loop attenuates structural oscillations sufficiently fast, the modeling of the remaining dynamics drastically simplifies. Consider a damped uniform cantilever as a model for an arbitrary link in the kinematic chain. As reported by Meirovitch [2001], the assumption of small deflections renders the deflection differential equations linear. Hence, the load torque distribution along the beam can be described by the superposition of three general components:

$$\tau_L(x) = \tau_\rho(x) + \tau_f(x) + \tau_\tau(x). \tag{1}$$

The summand $\tau_\rho(x)$ describes the load torque due to link mass per unit length ρ_b:

$$\tau_\rho(x) = \rho_b \frac{L^2}{2EI}\left(1 - 2\frac{x}{L} + \left(\frac{x}{L}\right)^2\right). \tag{2}$$

In this equation E denotes the Youngs modulus, I is the area moment of inertia about the bending axis and L denotes the link length.

A load force f_L at the tip causes a linear load torque distribution $\tau_f(x)$:

$$\tau_f(x) = f_L \frac{L}{EI}\left(1 - \frac{x}{L}\right), \tag{3}$$

where L represents the beam length.

Next, a load torque τ_b acting on the tip results in a constant torque distribution $\tau_\tau(x)$ along the cantilever:

$$\tau_\tau(x) = \tau_b. \tag{4}$$

The equations (1) to (4) are qualitatively illustrated in fig. 4.

The equations of motion for conventional rigid robot arms are formulated with respect to torque acting at the joint shaft $\tau_J = \tau_L(0)$. Again, assuming small deflections, the link surface strain measured at a location x_s is caused by the load torque $\tau_L(x_s)$ as described in equation (1):

$$\tau_L(x_s) = \frac{EI}{y_b}\varepsilon(x_s), \tag{5}$$

where y_b is the distance between the link surface and the neutral fibre. Both torques differ by $\Delta\tau$:

$$\Delta\tau = \tau_L(0) - \tau_L(x_s) = \frac{\rho_b}{EI}\left(L\,x_s - \frac{1}{2}x_s^2\right) + \frac{f_L}{EI}x_s. \tag{6}$$

In the case of a constant payload and without possibly varying external contact forces, the load force f_L and, along with that, the difference $\Delta\tau$ is constant up to a scaling due to the link orientation with respect to gravity. The linear mapping:

$$\tau_J = \frac{EI}{y_b}\varepsilon(x_s) + \Delta\tau \Leftrightarrow \varepsilon(x_s) = \frac{y_b}{EI}\left(\tau_J - \Delta\tau\right) \tag{7}$$

transforms the link strain $\varepsilon(x_s)$ measured near the joint into the load torque τ_J acting upon the joint shaft and vice versa. Hence, the links with the applied strain gauges act as load side joint torque sensors. It allows to identify the arm dynamics irrespective of the joint properties such as highly nonlinear and time variant joint friction.

Applying equation (7) for each joint-link-module, the damped arm dynamics can be directly expressed with reference to the link strains using the same mathematical structure known from the joint torque referred dynamics of conventional rigid robots:

$$\boldsymbol{\varepsilon}(\mathbf{x}_s) = \mathbf{I}_\varepsilon(\mathbf{q})\ddot{\mathbf{q}} + \mathbf{C}_\varepsilon(\mathbf{q},\dot{\mathbf{q}})\dot{\mathbf{q}} + \mathbf{g}_\varepsilon(\mathbf{q}), \tag{8}$$

with

$$\mathbf{I}_\varepsilon = \mathbf{K}_b\,\mathbf{I}, \qquad \mathbf{C}_\varepsilon = \mathbf{K}_b\,\mathbf{C}, \tag{9}$$

$$\mathbf{g}_\varepsilon = \mathbf{K}_b\,\left(\mathbf{g} - \mathrm{diag}\left(\Delta\boldsymbol{\tau}_i\right)\right), \qquad \mathbf{K}_b = \frac{y_b}{EI}\,\mathbf{E}. \tag{10}$$

Therein $\mathbf{I}$ denotes the symmetric positive definite robot inertia matrix. The matrix $\mathbf{C}$ collects the Coriolis and centrifugal terms. The vector $\mathbf{g}$ describes the gravitational joint load. The vector $\boldsymbol{\varepsilon}(\mathbf{x}_s)$ holds the strains $[\varepsilon_2,\,\varepsilon_3]^\mathrm{T}$ measured at each joint-link-module. The $\Delta\tau_i$ are the corresponding torque offsets. $\mathbf{E}$ is the unit matrix.

The equation (8) is linear in the parameters. It can be rearranged as the linear regression problem:

$$\boldsymbol{\varepsilon} = \mathbf{Y}_\varepsilon(\mathbf{q},\dot{\mathbf{q}},\ddot{\mathbf{q}})\,\boldsymbol{\chi}_\varepsilon, \tag{11}$$

in which only the realized joint motion influences the regressor $\mathbf{Y}_\varepsilon$ and $\boldsymbol{\chi}_\varepsilon$ is the minimal set of identifiable base dynamics parameters. This work follows the numerical approach from Khalil and Dombre [2004] to find these parameters, wich analyzes the space spanned by the columns of $\mathbf{Y}_\varepsilon$. Subsequent to the reduction, equation (11) is solved for $\boldsymbol{\chi}_\varepsilon$ in the least-squares sense.

The joint trajectory has to be designed to sufficiently excite the arm dynamics. In this work amplitude-modulated pseudo-random binary signals (APRBS, see [Isermann and Münchhof, 2011, p. 174]) serve as stimuli for each individual joint. The realizations exemplified in fig. 5 (**a**) are based on a $\sin^2$ acceleration profile and exhibit satisfactory condition numbers and smallest singular values for $\mathbf{Y}_i$ and $\mathbf{Y}_\varepsilon$. Ten identification data sets are recorded for each payload between $m_L = 0 \ldots 400$ g and randomly split into 50 % for identification as well as 50 % for validation. Each stimulus has a duration of 80 s and recorded at a sampling rate of 100 Hz and subsampled to 20 Hz for identification. The stimuli are executed on the second and third joint simultaneously and cover their whole operating range. This contribution concentrates on the exploitation

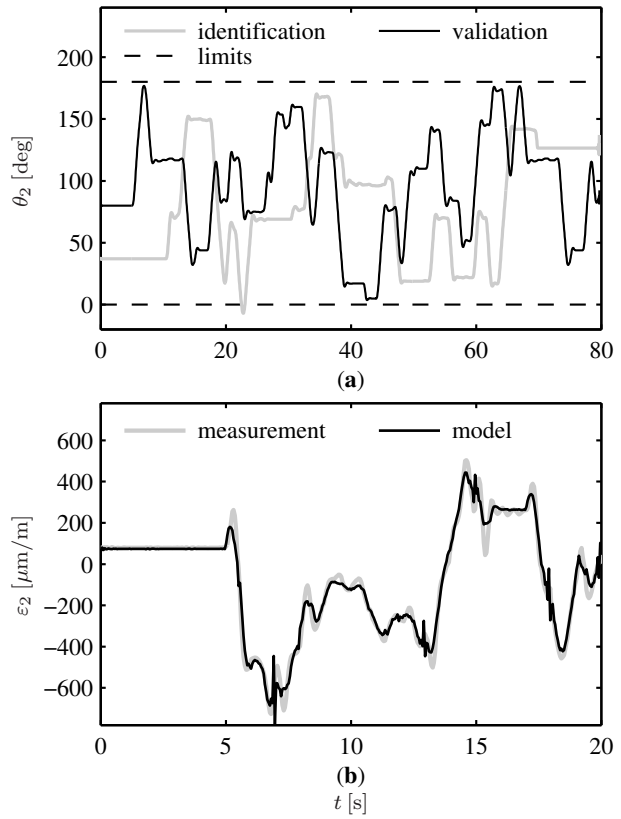

Fig. 5. Joint angle stimulus responses (**a**) exemplified for the identification and the validation data set (payload of 400 g). Close-up to a strain dynamics validation result obtained for the second link (**b**).

of the intrinsic link compliance so that the first joint is kept fixed at the zero position without loss of generality. The maximum acceleration is 200 deg/s^2. The maximum speed is 70 deg/s.

The joint velocities and accelerations are obtained from numerical differentiation and filtering with a first order filter. The filter cut-off frequencies are 80 Hz for the velocity and 20 Hz for the subsequent acceleration filtering.

The close-up to a strain identification result is illustrated in fig. 5 (**b**) for the worst scenario with a payload mass of 400 g. Deviations between the measurement and the model output mainly emerge due to measurement noise as well as only partially explained large strain peaks during rapid motion reversal with the high payload. In total, the normalized root mean squared error ranges between 9.5 % without payload and 22.2 % with a payload of 400 g. The results prove the validity of the model derivation in the previous subsection. The model accuracy is conspicuously sufficient for the collision detection and reaction in the next section. In fact, model errors and damping imperfections basically limit the collision detection sensitivity.

5. COLLISION DETECTION

With the identified damped strain dynamics model the straightforward choice of a residual vector for collision detection is the difference between the measurement and the model output:

$$\mathbf{r}_\varepsilon = \boldsymbol{\varepsilon} - \mathbf{I}_\varepsilon(\mathbf{q})\ddot{\mathbf{q}} - \mathbf{C}_\varepsilon(\mathbf{q},\dot{\mathbf{q}})\dot{\mathbf{q}} - \mathbf{g}_\varepsilon(\mathbf{q}). \tag{12}$$

A collision is detected, if the absolute value of any element in $\mathbf{r}_\varepsilon$ exceeds a threshold. Prediction errors define the individual detection sensitivity. Collision isolation can be achieved by determination of the last link in the open kinematic chain showing a threshold violation. The sign of the residual carries the directional information.

The drawback of the direct strain residual is the necessity to compute the joint acceleration in the presence of measurement noise. Luca and Mattone [2005] propose an alternative approach based on the generalized momentum of the robot arm. The generalized momentum $\mathbf{p}$ is the product of the robot inertia matrix and the joint velocity vector. Using the linear relation (7) the strain based equivalent to the generalized momentum is defined analogously:

$$\mathbf{p}_\varepsilon = \mathbf{I}_\varepsilon(\mathbf{q})\dot{\mathbf{q}}. \tag{13}$$

With $\dot{\mathbf{I}}_\varepsilon(q) = \mathbf{C}_\varepsilon(\mathbf{q},\dot{\mathbf{q}}) + \mathbf{C}_\varepsilon^{\mathrm{T}}(\mathbf{q},\dot{\mathbf{q}})$ the temporal derivative of the generalized momentum (13) computes to:

$$\dot{\mathbf{p}}_\varepsilon = \boldsymbol{\varepsilon} + \mathbf{C}_\varepsilon^{\mathrm{T}}(\mathbf{q},\dot{\mathbf{q}})\dot{\mathbf{q}} - \mathbf{g}_\varepsilon(\mathbf{q}). \tag{14}$$

The residual is thus defined by the difference between the directly computed generalized momentum (13) and the generalized momentum obtained from integration of equation (14):

$$\mathbf{r}_p = \mathbf{K}_I \left[\mathbf{p}_\varepsilon - \int_0^t \boldsymbol{\varepsilon} + \mathbf{C}_\varepsilon^{\mathrm{T}}(\mathbf{q},\dot{\mathbf{q}})\dot{\mathbf{q}} - \mathbf{g}_\varepsilon(\mathbf{q})\mathrm{d}t - \mathbf{p}_\varepsilon(0)\right], \tag{15}$$

where $\mathbf{K}_I$ is a positive diagonal gain matrix. Let the measured strain vector $\boldsymbol{\varepsilon}$ be the superposition of the nominal collision free strain $\boldsymbol{\varepsilon}_f$ and the collision strain $\boldsymbol{\varepsilon}_c$. Following Luca and Mattone [2005] with $\mathbf{p}_\varepsilon(0) = 0$, the first order residual dynamics compute to:

$$\dot{\mathbf{r}}_p = -\mathbf{K}_I\,\mathbf{r}_p + \mathbf{K}_I\,\boldsymbol{\varepsilon}_\boldsymbol{c}. \tag{16}$$

Rewriting this expression (16) into a transfer function for the i-th element in $\mathbf{r}_p$ corresponding the i-th robot joint:

$$r_{p,i} = \frac{K_{I,i}}{s + K_{I,i}}\,\varepsilon_{c,i} \tag{17}$$

reveals, that the residual is the filtered version of the collision strain. The filter constants are tuned through $\mathbf{K_I}$. They trade off the detection reactiveness and noise sensitivity. The modeling accuracy has the main impact on the collision detection sensitivity. Adaptive thresholding has been proposed by Luca and Mattone [2004]. In this work the detection thresholds are chosen to be six times the standard deviation of the residuals computed on the identification and validation data. The isolation of the collided link is identical to the direct strain residual $\mathbf{r}_\varepsilon$ discussed before.

6. COLLISION REACTION

The collision reaction in this work is implemented on the velocity controller level. Once a collision is detected, the nominal reference for the velocity controller is immediately replaced by the reaction velocity $\dot{q}_{c,i}$. The simplest reaction strategy is to just stop by commanding zero velocity in each joint. Using the collision information contained in the strain referred generalized momentum based residual,

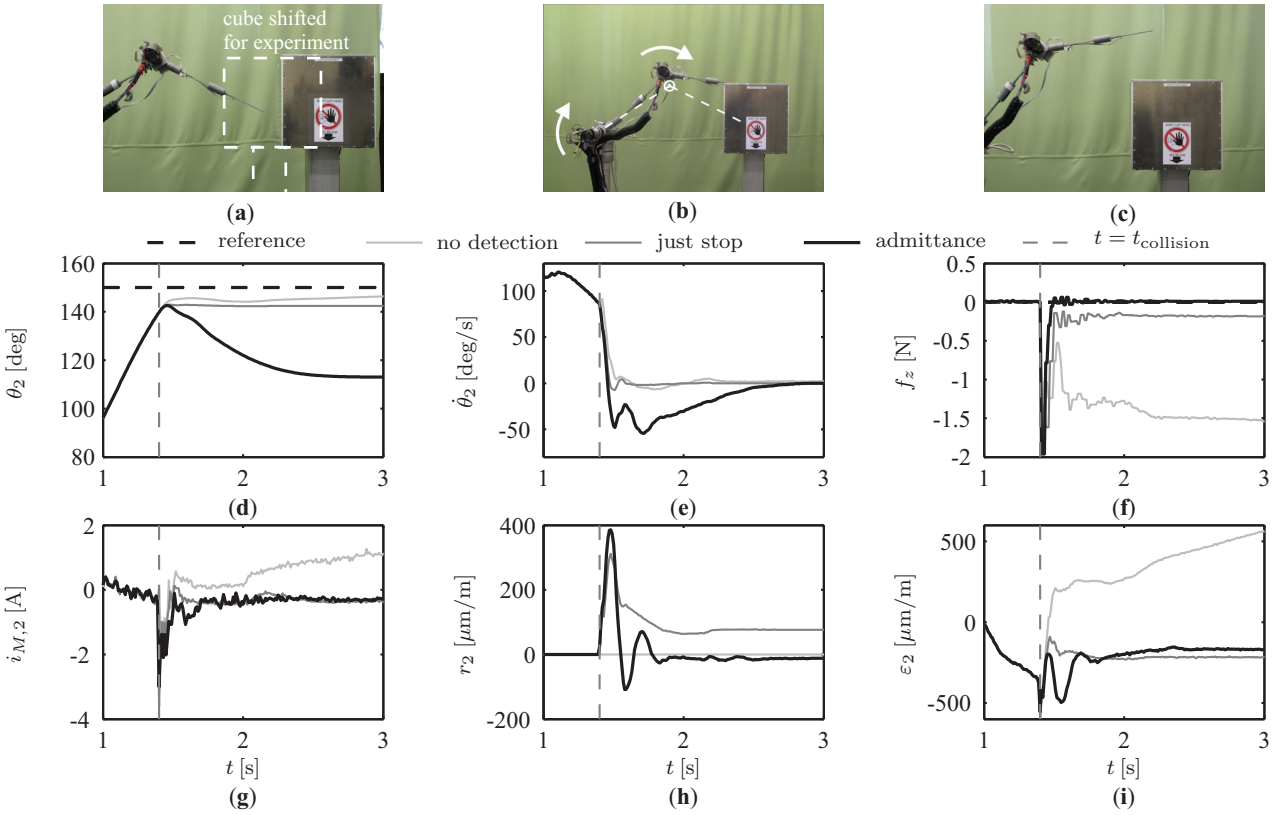

Fig. 6. *Blunt* impacts with the contact cube. The commanded pose (**a**) with the contact cube shifted aside, the collision instant (**b**) with commanded pose sketched inside the cube as well as the rest position after collision reaction using the admittance-strategy (**c**). Time series plots of the second joint angle (**d**), angular velocity (**e**), the normal force f_z at the contact cube, the current (**g**), the residual (**h**) and the strain (**i**) on the second link.

an admittance strategy is realized alternatively. Equation (17) implies that the residual has the dimension of strain, which according to expression (5) is equivalent to a load torque acting on the i-th joint-link-module. The generic collision admittances A_i for the each i-th joint:

$$A_i(s) = \frac{\dot{q}_{c,i}(s)}{r_{p,i}(s)} = \frac{k_{o,i}}{m_{c,i}\, s + f_{c,i} + k_{c,i}/s}, \qquad (18)$$

with $m_{c,i}$, $f_{c,i}$ and $k_{c,i}$ being the inertial, resistive and capacitive components allow to arbitrarily shape the reaction behavior. In this work a reflex strategy is used based on small parameters $m_{c,i}$ and $f_{c,i}$ as well as $k_{c,i} = 0$ and an overreaction gain $k_{o,i} \geq 1$.

Fig. 6 contains the collision detection and reaction results for blunt impacts with the contact cube. The maximum velocity is 100 deg/s, the joint acceleration is 200 deg/s^2. The commanded joint configuration corresponds to an end effector pose within the contact cube as indicated in fig. 6 (**a**) and (**b**). Without collision detection, the joint controller steadily minimizes the angular pose error by increasing the motor current, which leads to a drastical link deformation (fig. 6 (**i**)). With activated collision detection using the stop strategy the robot halts within 8 ms. The over- and undershoot visible in fig. 6 (**e**) originates from the oscillation damping. The residual contact force measured at the cube amounts to 0.17 N. The overreactive admittance strategy causes the robot to emmediately retreat after collision. Again the oscillation damping action is clearly visible. The robot comes to a rest in the pose visible in fig. 6 (**c**). The rest pose is defined by the inertial and resistive parameters in A_i.

In the experiment shown in fig. 7 the robot periodically moves between the two joint configurations $\boldsymbol{\theta} = [0° \; 45° \; -45°]^{\mathrm{T}}$ and $\boldsymbol{\theta} = [0° \; 135° \; 45°]$. At second 5.17 (fig. 7 (**d**)) a human enters the workspace and interrupts this motion. After the reflex reaction (fig. 7 (**e**)) the overreaction gains $k_{o,i}$ are set to 1. The low friction and low inertia render the robot easily backdrivable and reconfigurable by physical interaction at any point along the kinematic structure. Such an interaction is illustrated in fig. 7 (**f**)-(**i**).

7. CONCLUSIONS AND OUTLOOK

The paper experimentally shows that the strain referred dynamics of an actively damped multi-elastic-link robot arm with uniform links are governed by exactly the same model structure as the joint current referred model known from conventional rigid robots. This enables the usually avoided link elasticity to be exploited for collision detection, reaction and human robot interaction. The direct applicability of the generalized momentum based concept proposed by Luca et al. [2006] has been proven through blunt collision experiments with force sensor as well as task interruption and kinesthetic reconfiguration by a human operator. More experiments including sharp impacts

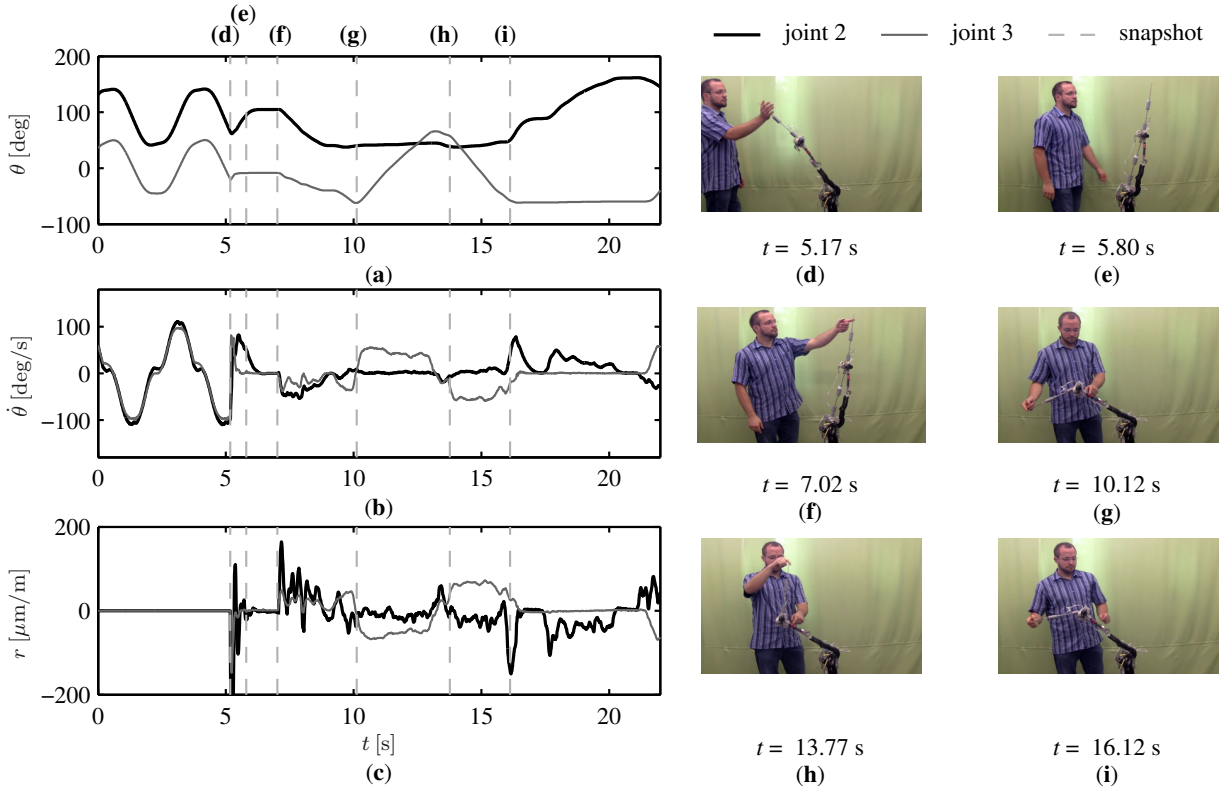

Fig. 7. Physical interaction with a human. Measurements for the joint angles (**a**), joint velocities (**b**) and residuals (**c**) along with snapshots of particular instants during the interaction (**d**)-(**i**).

with fragile objects and a human arm are provided in a supporting **video** [1] . In summary the link elasticity is not ultimately "just a problem". The contribution shows: with the detrimental effects cancelled it can become a promising new perspective for contact sensing, physical interaction and force control.

Short term research is concerned with direct force control as well as the online-load estimation based on the damped arm dynamics. A long-term objective is to apply the presented concept to a setup with more degrees of freedom and multiple planes of oscillation.

REFERENCES

C. Behn, T. Schmitz, H. Witte, and K. Zimmermann. Animal Vibrissae: Modeling and Adaptive Control of Bio-inspired Sensors. In *Advances in Computational Intelligence*, pages 159–170. Springer, 2013.

M. Benosman and G. Le Vey. Control of flexible manipulators: A survey. *Robotica*, 22(5):533–545, 2004.

S. Haddadin, A. Albu-Schaeffer, and G. Hirzinger. The Role of the Robot Mass and Velocity in Physical Human-Robot Interaction - Part II: Constrained Blunt Impacts. In *International Conference on Robotics and Automation*, pages 1339–1345, 2008.

R. Isermann and M. Münchhof. *Identification of dynamic systems: An introduction with applications*. Springer, Heidelberg and New York, 2011. ISBN 3540788786.

W. Khalil and E. Dombre. *Modeling, identification and control of robots*. Butterworth-Heinemann, 2004.

[1] http://youtu.be/kJPuenyxeps

A. de Luca and R. Mattone. An adapt-and-detect actuator FDI scheme for robot manipulators. In *International Conference on Robotics and Automation*, volume 5, pages 4975–4980, 2004.

A. de Luca and R. Mattone. Sensorless robot collision detection and hybrid force/motion control. In *International Conference on Robotics and Automation*, pages 999–1004, 2005.

A. de Luca, A. Albu-Schaffer, S. Haddadin, and G. Hirzinger. Collision detection and safe reaction with the DLR-III lightweight manipulator arm. In *International Conference on Intelligent Robots*, pages 1623–1630. IEEE/RSJ, 2006.

J. Malzahn and T. Bertram. Dynamics Identification of a Damped Multi Elastic Link Robot Arm under Gravity. In *International Conference on Robotics and Automation*, 2014.

J. Malzahn, A. S. Phung, F. Hoffmann, and T. Bertram. Vibration control of a multi-flexible-link robot arm under gravity. In *International Conference on Robotics and Biomimetics*, pages 1249–1254, 2011.

T. Mansour, X. Jiang, A. Konno, and M. Uchiyama. Experimental verification on vibration suppression of a flexible manipulator using MPID controller. In *International Conference on Robotics and Automation*, pages 2896–2901. IEEE, 2008.

L. Meirovitch. *Fundamentals of vibrations*. McGraw-Hill, Boston, 2001. ISBN 9780072881806.

L. Miersch et al. Flow sensing by pinniped whiskers. *Philosophical Transactions of the Royal Society B: Biological Sciences*, 366(1581):3077–3084, 2011.